PAPER • OPEN ACCESS

Numerical simulation of shear driven film instability over heterogeneous surfaces via enhanced lubrication theory

To cite this article: Nicola Suzzi and Giulio Croce 2024 *J. Phys.: Conf. Ser.* **2685** 012019

View the article online for updates and enhancements.

Numerical simulation of shear driven film instability over heterogeneous surfaces via enhanced lubrication theory

Nicola Suzzi[1] **and Giulio Croce**[1]

[1]DPIA - Dipartimento Politecnico di Ingegneria e Architettura - Universitá di Udine - Via delle Scienze - 33100 - Udine (UD) - Italy

E-mail: `nicola.suzzi@uniud.it`, `giulio.croce@uniud.it`

Abstract. The prediction of the transition between continuous film, ensemble of rivulets and moving droplets is crucial in applications such as in-flight icing on airfoil wings or a number of chemical reactors. Here, lubrication theory is used to numerically investigate the stability of a continuous liquid film, driven by shear, over a heterogeneous surface. The disjoining pressure is used to model surface wettability, while the full implementation of the film curvature allows to investigate contact angles up to $60°$. Different heterogeneous surface configurations occurring in real problems are investigated. An extended computational campaign records the transition from continuous film to rivulet regime and, if present, the further transition from rivulet to droplets at different flow conditions. A moving grid approach allows for accurate prediction of instability phenomena at low computational cost. The numerical results are successfully validated with experimental evidence in case of critical flow rate leading to a stable dry patch and compared with literature results involving the inherently multiscale in-flight icing phenomenon, providing useful statistical information, required to transfer the present detailed small-scale information into larger scale CFD computational approaches.

1. Introduction

The evolution of a liquid layer over a solid substrate is involved in several engineering applications. In in-flight icing phenomenon over airfoil wings, supercooled droplets from the clouds deposit on wing surface, forming a thin liquid layer, which evolution affects the ice accretion and, thus, the surface roughness, which in turn may influence the airfoil aerodynamics [1–3]. In CO_2 absorption through structured packing a liquid solvent flows down corrugated layers, while gas CO_2 flows up. Maximizing the liquid-gas interface area allows to enhance the absorption process [4,5].

Film instability phenomenon has been largely investigated both numerically [4,6–12] and experimentally [13, 14]. In particular, finger instability of a film falling down an inclined plate with non-uniform contact angle, modeled through disjoining pressure in accordance with the precursor work of [15], was numerically investigated via lubrication theory in [6], where the effect of solid substrate on the film morphology was investigated. The effect of a solid occlusion on an advancing film front was numerically investigated by [16] via lubrication theory, with the liquid bulk that may cross the occlusion and wet the whole domain or form a stable dry-patch, depending on contact angle and flow condition. A dry-patch over a continuous film falling down an inclined plate was experimentally generated via a small perturbation in the liquid bulk and the critical flow rate leading to dry-patch shedding was traced under different flow conditions in [13, 14]. If gravity driven films, typical of chemical and heat transfer related applications, have been largely investigated, little information is available for shear driven films [17, 18], as those encountered in in-flight icing conditions. Nonetheless, the prediction of transition between

film and rivulets in an icing environment affects the length of the potentially iced region, as well as the transient evolution of the accreted ice shape, and is thus an important feature to be considered. Here, in order to fill this gap, a shear driven film is numerically investigated under lubrication theory. The full implementation of capillary pressure allows to investigate contact angles up to $\theta = 60°$ [9], while small-slope approximation leads to inaccurate results for $\theta \geq 30°$ [9, 19]. Furthermore, a moving grid approach is adopted, in order to catch instabilities occurring far downstream with low computational cost. As the flow regime play a crucial role in both in-flight icing and CO_2 absorption, finger instability of an advancing film, driven by shear over an initially dry domain, is investigated, with the aim of identifying thresholds between continuous film and rivulet regimes. An application to the water film around an airfoil provides a first validation of the procedure. Furthermore, the stability of a continuous flat film, which initially wet the whole domain, is also investigated, introducing a small perturbation, that may induce a stable dry-patch or the de-wetting of the whole domain, with transition to droplet regime. The presented results can be used for developing simplified models, that does not go into the details of the film length scale.

2. Mathematical model

Consider a thin film flowing over a flat plate, driven by shear. Let $\boldsymbol{\tau}$ be the shear, applied at liquid-gas free surface, h_0 and u_0 the undisturbed film thickness and velocity, calculated according to Nusselt theory as $u_0 = \tau h_0/(2\mu)$. Lubrication theory allows to integrate the continuity equation along the plate normal direction. Assuming that the coordinate system moves with a constant velocity $\mathbf{u}^*$, retaining the viscous dissipation terms arising from velocity gradient across the film thickness and neglecting liquid inertia, the momentum equation gives a parabolic velocity profile. Averaging the film velocity and substituting in the continuity equation gives the well known lubrication equation for a shear driven film:

$$\frac{\partial h}{\partial t} - \mathbf{u}^* \cdot \nabla h + \nabla \cdot \left(\frac{\boldsymbol{\tau} h^2}{2\mu} - \frac{\nabla p}{3\mu} h^3 \right) = 0, \ p = -2\sigma\kappa - D, \tag{1}$$

where the liquid pressure p is given by the sum of capillary pressure and disjoining pressure. The free surface curvature is equal to,

$$2\kappa = \frac{\left[1 + \left(\frac{\partial h}{\partial y}\right)^2\right]\frac{\partial^2 h}{\partial x^2} + \left[1 + \left(\frac{\partial h}{\partial x}\right)^2\right]\frac{\partial^2 h}{\partial y^2} - 2\frac{\partial h}{\partial x}\frac{\partial h}{\partial y}\frac{\partial^2 h}{\partial x \partial y}}{\left[1 + \left(\frac{\partial h}{\partial x}\right)^2 + \left(\frac{\partial h}{\partial y}\right)^2\right]^{3/2}}, \tag{2}$$

while the disjoining pressure term is equal to [6],

$$D = B\left[\left(\frac{d}{h}\right)^n - \left(\frac{d}{h}\right)^m\right], B = \frac{\sigma}{d}\frac{(n-1)(m-1)}{n-m}(1-\cos\theta), \tag{3}$$

where $n > m > 1$ and $d \ll h_0$ is the precursor film thickness.

Assuming that shear is directed over y, which means $\boldsymbol{\tau} = \tau\hat{\mathbf{j}}$, introducing the capillary number of the undisturbed film as $Ca = \mu u_0/\sigma$ and defining the following non-dimensional quantities,

$$H = \frac{h}{h_0}, \delta = \frac{d}{h_0}, \mathbf{X} = \frac{\mathbf{x}}{L_0}, \mathbf{U} = \frac{\mathbf{u}}{u_0}, T = \frac{t}{(L_0/u_0)},$$

$$P = \frac{p}{\left(\sigma h_0/L_0^2\right)}, 2K = \frac{2\kappa}{\left(h_0/L_0^2\right)}, \Pi = \frac{D}{(\sigma/h_0)}, \tag{4}$$

with L_0 being the characteristic length scale, $L_0 = h_0\left(3\,Ca\right)^{-1/3}$, the governing lubrication equations can be recast in non-dimensional form,

$$\frac{\partial H}{\partial T} - \mathbf{U}^* \cdot \nabla H + \nabla \cdot \left(H^2\hat{\mathbf{j}} - H^3\nabla P\right) = 0, \ P = -2K - \frac{\Pi}{\left(3\,Ca\right)^{2/3}}, \tag{5}$$

where the non-dimensional free surface curvature is:

$$2K = \frac{\left[1+(3\,\text{Ca})^{2/3}\left(\frac{\partial H}{\partial Y}\right)^2\right]\frac{\partial^2 H}{\partial X^2} + \left[1+(3\,\text{Ca})^{2/3}\left(\frac{\partial H}{\partial X}\right)^2\right]\frac{\partial^2 H}{\partial Y^2} - 2\,(3\,\text{Ca})^{2/3}\frac{\partial H}{\partial X}\frac{\partial H}{\partial Y}\frac{\partial^2 H}{\partial X\partial Y}}{\left[1+(3\,\text{Ca})^{2/3}\left(\frac{\partial H}{\partial X}\right)^2+(3\,\text{Ca})^{2/3}\left(\frac{\partial H}{\partial Y}\right)^2\right]^{3/2}}. \tag{6}$$

Eqs. (5) and (6) were numerically solved on an orthogonal, structured grid of $N_x \times N_y$ elements via Finite Volume Method (FVM), using an in-house code, previously developed in `FORTRAN` language and largely validated by the Authors [9,11]. Spatial discretization was achieved via the second order centered scheme of [20], while Alternating Direction Implicit (ADI) approximate factorization of [21] was implemented for marching in time. Parallelization for shared memory machines was implemented using `OpenMP` in order to speed up computations.

3. Problem statement

3.1. Non-wettable patch array

As a first case, we evaluated the effect of a localized perturbation on the stability of an advancing film. In particular, a film front driven by shear was perturbed by an array of small, non-wettable square patches of non-dimensional pitch $L_p = 60$ along X and size $L_\theta = 1$. Different configurations were considered, in order to evaluate whether the instability triggered by the patch will increase or will dampen as the film flows downstream. Computations were run on a domain of size $L_X \times L_Y = 60 \times 60$. The film was initialized with the solution of an advancing 1D shear driven film, with contact line front located at $Y \sim L_Y/2$ (to do so, a preliminary computation on a uniform substrate had to be run, in order to get the shape of the interface of a 1D advancing film). Periodic boundary conditions were applied at $X = 0, L_X$. Inlet condition was applied through $Y = 0$, while fully developed flow was imposed through $Y = L_Y$. The non-wettable patch of size $L_\theta = 1$, with a 10% increased value of the contact angle, was initialized in the dry region of the computational domain. In order to follow finger instability further downstream of the generating patch, we use a relative frame of reference, moving along Y with the advection speed of the undisturbed film contact line, equal to $U^* = \left(1-\delta^3\right)/(1-\delta)$. Time marching was stopped when moving film front is affected by boundary conditions imposed through $Y = 0, L_Y$ (i.e. receding front close to inlet at $Y = 0$ and outlet section at $Y = L_Y$ reached by advancing front).

3.2. Heterogeneous surface

A second example considers a shear driven advancing film front over an heterogeneous surface, representative of a real fouled surface as usually encountered in real world environment, in particular on airfoil surfaces naturally exposed to external contamination. The contact angle variation, which follows,

$$\theta(X,Y) = \sum_{k=-n}^{+n}\sum_{j=-m_k}^{+m_k} \Theta_{j,k}\cos\left(2\pi\frac{X\cdot j + Y\cdot k}{L_\pi}+\Psi_{j,k}\right), m_k = \left\lceil m\left(1-\frac{k^2}{n^2}\right)\right\rceil, \tag{7}$$

is periodic over $L_\pi = 60$ with $m, n = 120$ and ranges in $\theta_0 \pm \Delta\theta$, with $\Delta\theta = 0.1\,\theta_0$. Domain size, boundary and initial conditions are defined as in section 3.1.

3.3. Dry-patch generation

Finally, a flat, continuous film initially wetting the whole domain, $H(X,Y)|_{T=0} = 1$, was perturbed via an array of small, localized square dry-patches of pitch $L_p = 60$ and size $L_\theta = 1$, characterized by an increased value of the contact angle (+10% of the base contact angle) and initialized in the computational domain, of size $L_X \times L_Y = 60 \times 60$. Boundary conditions are the same as in sections 3.1 and 3.2, while the moving grid velocity was set to zero, $U^* = 0$. When a stationary dry-patch hanging to the small non-wettable patch was detected, the latter was removed, checking if the stationary dry-patch slowly

shed away or remains stationary.

Two values of the reference contact angle, $\theta_0 = 30°, 45°$, were investigated for the three test cases, while the capillary number was ranged in Ca $\in \left[10^{-3}, 10^{-1}\right]$. Following [6], the precursor film thickness was set to $\delta = 5 \times 10^{-2}$ for all the computations. After a grid dependency analysis, the spatial discretization steps were set to $\Delta X, \Delta Y \leq 5 \times 10^{-2}$.

4. Result

4.1. Non-wettable patch array

Parametric computations were run, in case of an array of equally spaced small non-wettable patches on a hydrophilic surface, at $\theta_0 = 30°, 45°$ and capillary number ranging from Ca $= 0.1$ down to the critical value leading to rupture of the unperturbed 1D film front. Below Ca$_{cr}$, which depends on the substrate wettability, droplet regime is expected. Running preliminary computations of 1D shear driven film, it was found Ca$_{cr} = 10^{-2}$ for $\theta = 45°$ and Ca$_{cr} = 3 \times 10^{-2}$ for $\theta = 30°$. Then, the moving contact line was traced in the 2D computations, saving the curve (X_{cl}, Y_{cl}) at each time step. Both the advancing front and the receding front, computed as the topmost and the bottommost points of the contact line, were traced at each time step and used to estimate the receding and advancing contact line speed. Figures 1(a)
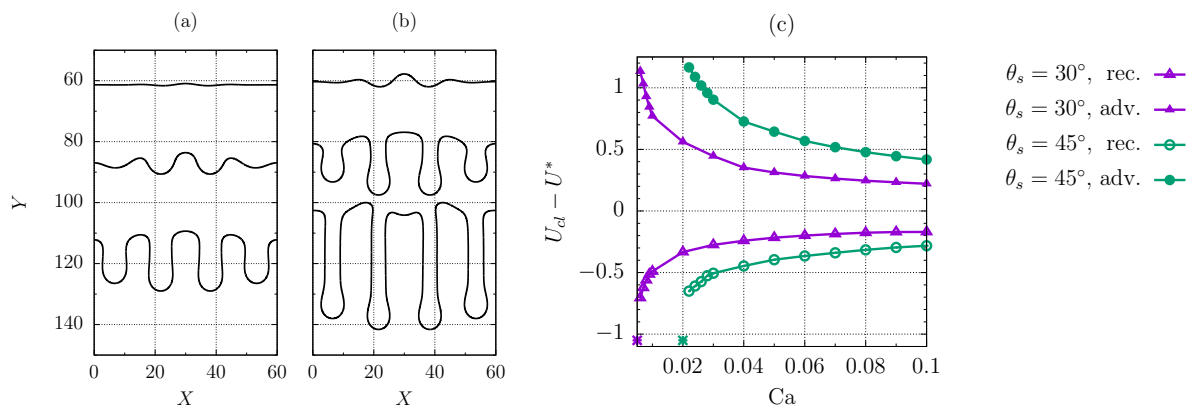

Figure 1. Moving contact line at different instants: $T = 25, 50, 80$. Ca $= 10^{-1}$, $\theta_0 = 30°$ (a); Ca $= 10^{-1}$, $\theta_0 = 45°$ (b). Relative velocity of advancing and receding fronts as a function of film capillary number, at $\theta_0 = 30°, 45°$ (c). Finger instability of the shear driven film is induced by an array of small non-wettable patches.

and 1(b) show the apparent contact line evolution after the film crossed the small non-wettable patch, at Ca $= 10^{-1}$ and different contact angles of the base surface. Note that the rivulets form far from the non-wettable patch, located at $Y \sim 30$, meaning that the moving greed approach is required. As expected, rivulets grow faster and have a narrower shape at increasing contact angle. Indeed, the stabilized speed of both the receding and the advancing fronts, plotted in figure 1(c), are higher when $\theta_0 = 45°$. Figure 1(c) also shows that rivulets grow faster at decreasing capillary number. Furthermore, it was observed that the receding front may hang on the small non-wettable patch even at Ca $>$ Ca$_{cr}$ (spare, star markers in figure 1(c)), demonstrating that the additional degrees of freedom of the 2D solution may anticipate the instabilities. However, we cannot derive general conclusions from such computations since the details of the non-wettable patch affects the final solution.

4.2. Heterogeneous surface

Parametric computations at $\theta_0 = 30°, 45°$ and Ca $\in \left[\text{Ca}_{cr}(\theta_0), 10^{-1}\right]$ were run in case of an heterogeneous surface, characterized by random variation of the contact angle. Figure 2(a) shows the

evolution of the contact line over the heterogeneous surface for $Ca = 10^{-1}$, $\theta_0 = 45°$. It is important to point out that the shape of the growing rivulets is qualitatively similar to figure 1(b), at same θ_0 and Ca, but the contact line looks more irregular due to random contact angle variation. Again, the contact line
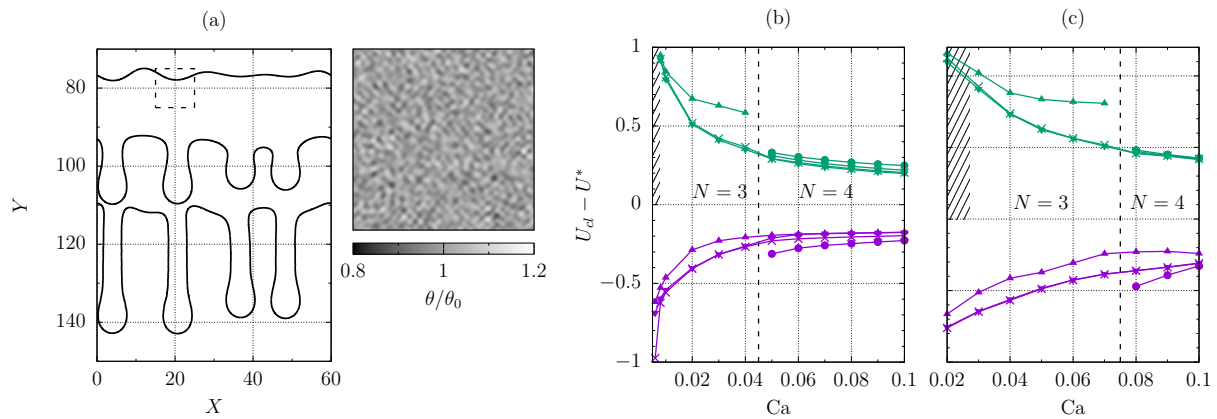

Figure 2. Moving contact line at $T = 42, 65, 88$ and zoom of the contact angle variation: $Ca = 10^{-1}$, $\theta_0 = 45°$ (a). Relative velocity of advancing (green) and receding (purple) fronts vs film capillary number (dotted region characterized by rupture of advancing front in droplets): $\theta_0 = 30°$ (b); $\theta_0 = 45°$ (c). Finger instability of the shear driven film is induced by an heterogeneous surface with $L_\pi = 60$.

was traced at each time step and the rivulets position tracked. The advancing speed of each rivulet front was computed as well as the receding speed of the valleys between neighbor rivulets, giving the velocity of the receding and the advancing fronts. Tracing only the topmost and the bottomest points would lead to scattered results, due to disturbance induced by a random contact angle variation. The rivulet advancing and receding speeds as a function of Ca are shown in figures 2(b) and 2(c). A bifurcation of the solution, with the number of stable rivulets passing from $N = 4$ to $N = 3$, can be observed: for $\theta_0 = 30°$ at $Ca \simeq 4 \times 10^{-2}$, figure 2(b); for $\theta_0 = 45°$ at $Ca \simeq 8 \times 10^{-2}$, figure 2(c). It is important to note that the number of stable rivulets is upper limited by $N \leq [L_\pi/\lambda]$, with $L_\pi \equiv L_X = 60$ and $\lambda = 9.4$ being the characteristic perturbance length from linear stability analysis [6]. Comparing figures 2(b) and 2(c), it can be observed that, at fixed Ca, a lower surface wettability leads to higher front speeds, meaning that rivulets grow faster at increasing θ_0. Receding fronts with $U_{rec} < 0$, which means that the film is not stable as the receding front goes upstream, were observed, for $\theta_0 = 30°$, at $Ca = 5 \times 10^{-3}$, still higher than $Ca_{cr} = 3 \times 10^{-3}$. Thus, an unstable film with rivulet front moving upstream may be observed at values higher that the critical one, derived from 1D analysis. The results, presented in figures 2(b) and 2(c), are useful for practical applications such as in-flight icing phenomenon on airfoil wings, where knowing the dynamic flow pattern evolution over the whole wing surface is crucial [2, 3]. As a proof of this, the numerical results of [3] were replicated: the critical thickness of a continuous water film on NACA0012 airfoil, leading to film break with transition to rivulet pattern, was evaluated from the critical capillary number as $h_{cr} = (2\,\sigma/\tau)\,Ca_{cr}$, with the local shear being estimated from the friction drag coefficient of the surrounding air flow, $\tau = \frac{1}{2}\rho_{air}\,c_f\,u_\infty^2$. The friction drag coefficient, figure 3(a), was derived from the CFD solution of a flow past NACA0012 airfoil at $Re = \rho_{air}\,u_\infty\,l_c/\mu_{air} = 1.7 \times 10^5$ and zero angle of attack. Flow field was computed via open source code SU2 on a quadrangular mesh of 230 336 nodes, using Spalart$-$Allmaras turbulence model. Figure 3(b) compares the computed critical film thickness as a function of chord position with literature data of [3], for an hydrophilic surface characterized by uniform contact angle $\theta = 30°$, showing good agreement.
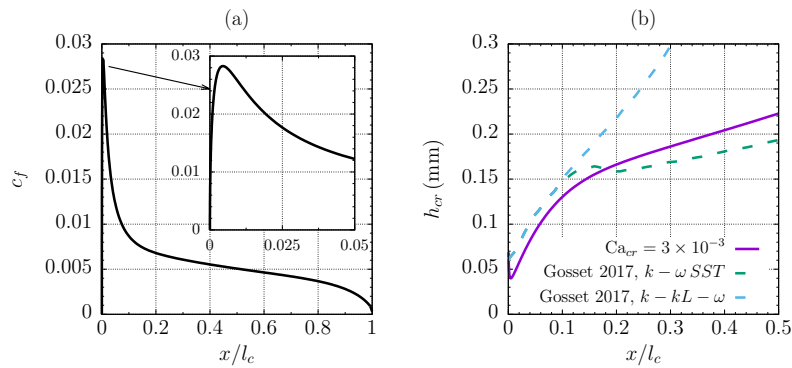
Figure 3. Friction drag coefficient as a function of chord position, air flow past NACA0012 airfoil at $Re = 1.7 \times 10^5$ (a). Critical film thickness leading to film-rivulet transition: numerical vs literature data from [3] (b). $l_c = 101\,\mathrm{mm}$, $u_\infty = 25\,\mathrm{m\,s^{-1}}$, $\theta = 30°$. Air and water properties evaluated at atmospheric pressure and temperature 20°C.

4.3. Dry patch generation

Dry-patch generation from a continuous film was investigated, at $\theta_0 = 30°, 45°$. The capillary number was varied, looking for the two critical cases: (1) a receding, unstable dry-patch, growing into rivulets and drops, forms at low values of Ca; (2) the perturbation does not induce the generation of a stationary dry-patch, leading to fully wetted domain at high values of Ca. The thresholds of Ca are shown in table 1. The

$\theta(°)$	$\mathrm{Ca} = \mu\, u_0 / \sigma$
	4×10^{-3}	5×10^{-3}	1×10^{-2}	2×10^{-2}	3×10^{-2}	4×10^{-2}
30	$*$	$\bullet$	$\bullet$	$\star$	$\star$	$\star$
45	$*$	$*$	$*$	$\bullet$	$\bullet$	$\star$

Table 1. Flow regimes: rivulets and moving droplets, $*$; stationary dry-patch, $\bullet$; fully wetted domain, $\star$. Small perturbation initialized in a flat, continuous film.

unstable dry-patch, growing into rivulets and droplets regime, was observed at $\theta_0 = 45°$ and $\mathrm{Ca} = 10^{-1}$, which is close to the critical value, leading to rupture of the 1D advancing film front. However, a receding contact line, with generation of rivulets and drops, was observed at $\mathrm{Ca} = 4 \times 10^{-3} > \mathrm{Ca}_{cr} = 3 \times 10^{-3}$ for $\theta_0 = 30°$. The threshold leading to fully wetted domain is not discussed, as it may be affected by the value of the increased contact angle, imposed inside the small perturbation. When a large, stationary dry-patch is generated, as in figure 4(a) for $\theta_0 = 45°$ and $\mathrm{Ca} = 3 \times 10^{-2}$, the small perturbation is removed, letting the dry-patch moving forward and slowly shed away, as shown in figure 4(b). In figure 5, referred to $\theta_0 = 45°$, $\mathrm{Ca} = 10^{-2}$, the evolution of the unstable dry-patch is followed: at the initial stage, a receding dry-patch is generated; however, after the moving contact line reaches the outlet section, finger instability is observed, with a rivulet forming in the core domain and breaking into droplets; then, further rivulets and droplets form, with the receding front of the main contact line approaching the inlet section.

The thresholds listed in table 1 can be compared with the experimental results of [13, 14]. In the experiments, a continuous film, driven by gravity, flowing down an inclined plate, which is fully wetted, was perturbed via a localized blow on the film, generating a stationary dry-patch. Then, the flow rate was slowly increased, until the dry-patch starts moving downstream. A critical flow rate per unit length Γ_{cr} was, thus, estimated in [13, 14]. Knowing fluid properties and applying Nusselt theory, $\Gamma_{cr} = \left(\rho\, g\, h_{cr}^3 \sin\alpha\right) / (3\mu)$ with α being the plate slope, the critical capillary number can be derived from Γ_{cr}. As clearly shown in table 2, the critical flow rates from [13, 14], experimentally derived from a similar test case and referred to contact angles that are close to the ones here investigated, fall inside the
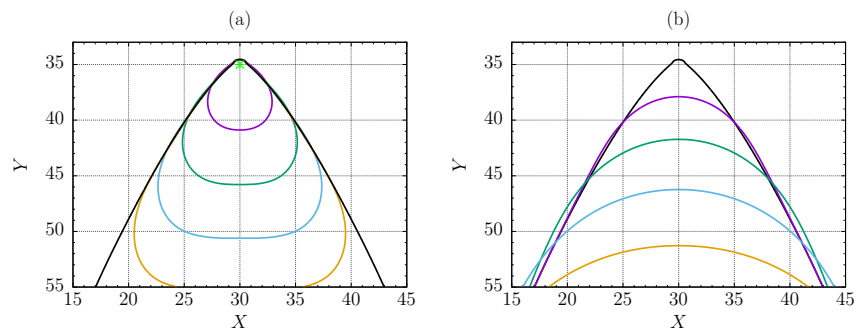
Figure 4. Contact line evolution: continuous film perturbed via localized non-wettable dry-patch, identified by a green marker, $T = 4, 8, 12, 16, 34$ (a); dry-patch shedding after non-wettable patch removal, $T = 34, 42, 49, 57, 64$ (b). $\theta_0 = 45°$, $\mathrm{Ca} = 3 \times 10^{-2}$.
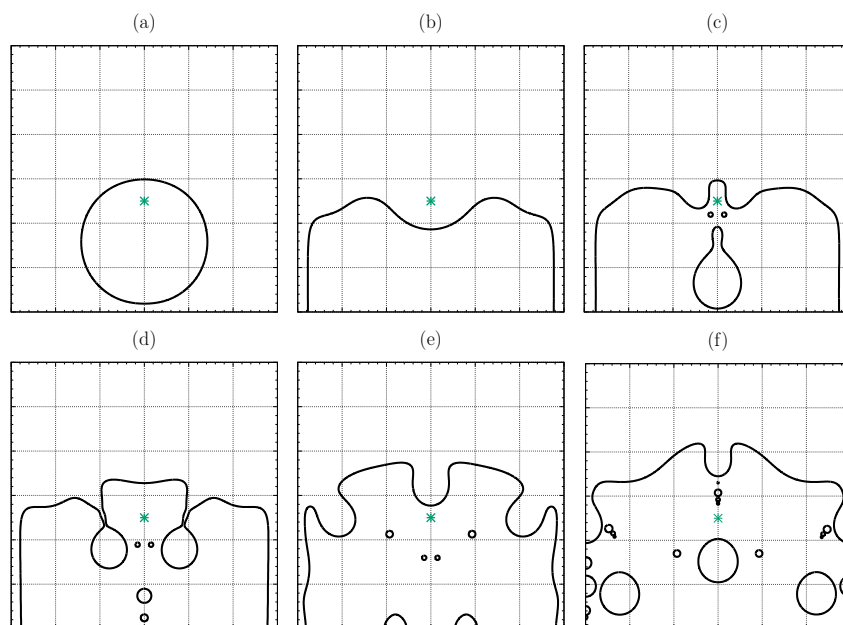

Figure 5. Contact line evolution at different instants: $T = 8$ (a); $T = 38$ (b); $T = 45$ (c); $T = 52$ (d); $T = 60$ (e); $T = 68$ (f). Continuous film perturbed via localized dry-patch, identified by a green marker. $\theta_0 = 45°$, $\mathrm{Ca} = 10^{-2}$, $L_X \times L_Y = 60 \times 60$.

α (deg)	θ (deg)	Γ_{cr} $(\mathrm{m}^2\,\mathrm{s})$	Ca_{cr}
90°	38° − 47°	3.5×10^{-6}	1.16×10^{-2}
90°	15° − 30°	$\sim 5 \times 10^{-7}$	3.18×10^{-3}

Table 2. Critical flow rate Γ_{cr} leading to shedding dry-patch in case of gravity driven film, from experimental results of [13, 14]. Silicone oil: $\rho = 950\,\mathrm{kg\,m^{-3}}$, $\mu = 0.019\,\mathrm{kg\,m^{-1}\,s^{-1}}$, $\sigma = 0.0206\,\mathrm{N\,m^{-1}}$.

numerical range of table 1.

5. Conclusion
Finger instability induced by non-uniform surface wettability and dry patch stability of a shear driven film were numerically investigated. The thresholds leading to transition between continuous film and

de-wetting regime, with the receding film replaced by droplets and rivulets, were found, in terms of critical capillary number of the undisturbed film. Slightly different Ca_{cr} were observed, depending on the investigated test case (unperturbed 1D advancing film, heterogeneous surface, dry-patch generation). However, the stability thresholds appear coherent with literature experimental evidence [13, 14] and numerical literature simulations [3], the latter based on a different approach in case of a film along an aircraft airfoil. Furthermore, the moving grid approach allowed to catch finger instability occurring late after the perturbation (single patch, heterogeneous surface) was introduced. The speeds of the advancing and receding rivulet fronts were computed, leading to useful information about the evolving flow pattern, to be used in simplified modelization of in-flight icing. The dry-patch stability analysis, which results are in good agreement with experimental literature [13, 14], is useful in applications as CO_2 absorption, where the stationary flow solution is required rather that its evolution in time. As a future work, further computations to better identify the thresholds between flow regimes will be run and the effect of the surface characteristics will be analysed. Furthermore, contact angle up to $60°$ and the combined effect of shear and gravity will be investigated.

References

[1] Croce G, De Candido E, Habashi W G, Munzar J, Aubé M S, Baruzzi G S and Aliaga C 2010 *Journal of Aircraft* **47** 1283–1289
[2] Zhang K, Wei T and Hu H 2015 *Experiments in Fluids* **56** 173
[3] 2017 *Prediction of rivulet transition in anti-icing applications*
[4] Hoffmann A, Ausner I, Repke J U and Wozny G 2005 *Computers & Chemical Engineering* **29** 1433
[5] Subramanian K and Wozny G 2012 *International Journal of Chemical Engineering* **2012** 838965
[6] Zhao Y and Marshall J S 2006 *Journal of Fluid Mechanics* **559** 355–378
[7] Shkadov V Y and Sisoev G M 2005 *Computers & Fluids* **34** 151–168
[8] Thiele U, Brusch L, Bestehorn M and Bar M 2003 *The European Physical Journal E* **11** 255–271
[9] Suzzi N and Croce G 2021 *Fluids* **21** 405
[10] Suzzi N and Croce G 2021 *Journal of Physics: Conference Series* **1868** 012010
[11] Suzzi N and Croce G 2019 *Physics of Fluids* **31** 122106
[12] Suzzi N and Croce G 2017 *Journal of Physics: Conference Series* **796** 012038
[13] Podgorski T, Flesselles J M and Limat L 1999 *Physics of Fluids* **11** 845
[14] Rio E and Limat L 2006 *Physics of Fluids* **18** 032102
[15] Schwartz L and Eley R 1998 *Journal of Colloid and Interface Science* **202** 173–188
[16] Sellier M 2015 *International Journal of Multiphase Flow* **71** 66–73
[17] Abas S S and Yatim Y M 2014 *Physics of Fluids* **1605** 361–366
[18] Sullivan J M, Wilson S K and Duffy B R 2006 *Process in Industrial Mathematics at ECMI 2006* **12** 774–778
[19] Perazzo C A and Gratton J *Journal of Fluid Mechanics* **507** 367–379
[20] Diez J A and Kondic L 2002 *Journal of Computational Physics* **183** 274–306
[21] Witelski T P and Bowen M 2003 *Applied Numerical Mathematics* **45** 331

Acknowledgments